RSC Advances

PAPER

View Article Online
View Journal | View Issue



Cite this: *RSC Adv.*, 2026, **16**, 13147

# Bandgap-engineered nitrogen plasma functionalized biochar-$TiO_2$ composite for enhanced antibiotic photodegradation

Rayhan Bin Masud,†[a] Samiha Raisa Alam,†[a] Hridoy Roy, †*[ab] Mohammad Jellur Rahman [c] and Md. Shahinoor Islam *[ad]

A nitrogen plasma-functionalized biochar-$TiO_2$ composite was engineered to enhance ciprofloxacin photodegradation by synergistically overcoming the inherent limitations of the wide bandgap and rapid charge recombination of $TiO_2$. Textile sludge-derived biochar, synthesized *via* pyrolysis, was integrated with sol–gel-prepared $TiO_2$ using the wet precipitation method. Subsequent AC plasma treatment achieved controlled nitrogen (N) doping without altering the crystalline structure. UV-vis DRS confirmed progressive bandgap narrowing from 3.10 eV (pristine $TiO_2$) to 2.90 eV (biochar-$TiO_2$) and further to 2.73 eV (plasma-doped composite), while EDX quantified effective N-incorporation (6.65 wt%) and XRD verified phase integrity. DLS analysis revealed reduced hydrodynamic diameters (90–106 nm) and suppressed agglomeration, which correlated with the hierarchical porosity observed in SEM, thereby enhancing reactive site accessibility. Photocatalytic evaluation across ciprofloxacin concentrations (10–50 mg $L^{-1}$) demonstrated exceptional performance; the plasma-doped composite achieved a 9-fold higher degradation rate (0.0196 $min^{-1}$ at 10 mg $L^{-1}$) than pristine $TiO_2$ and a 3-fold enhancement over non-plasma biochar-$TiO_2$. Remarkably, it maintained >40% superior efficiency at 50 mg $L^{-1}$ despite diffusion limitations. This enhancement is attributed to synergistic adsorption from the porous framework of biochar and bandgap-engineered reactive oxygen species (ROS) generation by plasma-induced Ti–O–N configurations. The proposed degradation mechanisms align with literature pathways involving decarboxylation and piperazine ring cleavage. The study establishes plasma-doped biochar-$TiO_2$ as an efficient photocatalyst for antibiotic remediation.

Received 1st December 2025
Accepted 1st March 2026

DOI: 10.1039/d5ra09288d

rsc.li/rsc-advances



## 1. Introduction

Pharmaceutical contaminants, including antibiotics, prescription drugs, and reproductive hormones, represent a significant class of aquatic pollutants that evade conventional wastewater treatment methods, such as coagulation, flocculation, and biodegradation.[1–3] Their persistence in groundwater and surface waters poses significant ecological and public health threats, primarily through the proliferation of antibiotic-resistant bacteria.[4–7] Advanced Oxidation Processes (AOPs) based on semiconductor photocatalysis offer a promising alternative, leveraging Reactive Oxygen Species (ROS) to mineralize persistent organic contaminants.[8–11] Among photocatalysts, titanium dioxide ($TiO_2$) is widely studied due to its stability, non-toxicity, and high redox potential.[12,13] However, its large bandgap (3.0–3.2 eV) restricts light absorption to the UV region, while rapid electron–hole recombination further limits practical efficiency.[14,15]

To enhance visible-light activity, nonmetal doping, *e.g.*, N, C, S, has been employed to narrow the bandgap of $TiO_2$ by introducing mid-gap states or modifying band edges.[16–18] Conventional doping methods, such as sol–gel and hydrothermal synthesis, however, often suffer from inhomogeneous dopant distribution, high energy consumption, and lengthy processing times.[19,20] Plasma doping has emerged as a scalable and energy-efficient alternative, enabling rapid, uniform dopant incorporation at low temperatures with minimal chemical waste.[21–24] Nitrogen plasma treatment, in particular, has demonstrated efficacy in reducing the bandgap of $TiO_2$ through the formation of Ti–O–N or Ti–N–O configurations;[25–27] however, the exact mechanistic role of nitrogen species remains under investigation.[28]

Concurrently, carbonaceous supports like biochar have been reported to be integrated with $TiO_2$ to further improve adsorption capacity and charge separation efficiency.[29–31] Biochar

[a]*Department of Chemical Engineering, Bangladesh University of Engineering and Technology, Dhaka 1000, Bangladesh. E-mail: shahinoorislam@che.buet.ac.bd; hridoyroy@che.buet.ac.bd*

[b]*Department of Chemical Engineering, University of Michigan, Ann Arbor, Michigan 48109, USA*

[c]*Department of Physics, Bangladesh University of Engineering and Technology, Dhaka 1000, Bangladesh*

[d]*Department of Textile Engineering, Daffodil International University, Dhaka 1341, Bangladesh*

† Authors contributed equally.

derived from waste biomass, such as textile sludge, offers a sustainable, low-cost material that also addresses waste management challenges in developing countries.[32–34] Despite these advances, the synergistic combination of plasma doping and biochar support has not been explored with a holistic approach. This is a critical oversight, as plasma functionalization could further enhance the interfacial interactions between $TiO_2$ and biochar, while biochar doping may amplify the benefits of nitrogen doping. Therefore, this work bridges these crucial aspects by utilizing AC plasma nitrogen doping of $TiO_2$ supported on textile sludge-derived biochar.

In this research, $TiO_2$, biochar composites, and plasma-doped variants were synthesized for multiscale characterization (morphology through SEM/EDX, crystallinity by XRD, sizing using DLS, and band structure utilizing UV-vis DRS). Synergistic bandgap modulation from biochar integration and dopant-induced electronic transitions was quantified. In addition, photocatalytic efficacy through ciprofloxacin degradation kinetics across concentrations (10–50 mg $L^{-1}$) was evaluated. This approach establishes plasma-functionalized biochar-$TiO_2$ as an efficient, sustainable photocatalyst while resolving fundamental structure–activity relationships in doped semiconductor systems.

## 2. Materials and methodology

### 2.1 Synthesis of $TiO_2$

$TiO_2$ was synthesized following the sol–gel method. Briefly, 100 mL of absolute ethanol and 60 mL of deionized (DI) water were mixed under magnetic stirring. Titanium isopropoxide (TTIP, 97%, 15 mL) was added dropwise to the solution under a fume hood, inducing turbidity indicative of $TiO_2$ formation. After 10 min stirring at room temperature (25 ± 2 °C), the pH was adjusted to 3.0, followed by 3 h continuous stirring. The suspension was then dried at 110 °C for 24 h, yielding a white powder that was calcined at 400 °C for 2 h in a muffle furnace (Model L 3/11, Nabertherm GmbH, Germany) with a heating rate of 5 °C $min^{-1}$, and subsequently ground to fine particles.

### 2.2 Synthesis of textile sludge biochar (TSB)

Dried textile sludge (≤1–2% moisture) was sourced from a wastewater treatment facility of a ready-made garment (RMG) manufacturer in Bangladesh. The sludge was ground and sieved (18–35 mesh) to isolate 0.5–1 mm particles. Pyrolysis was conducted under continuous $N_2$ flow (10 L $min^{-1}$) at 500 °C for 2 h (10 °C per min ramp) in a muffle furnace. The resulting biochar was then acid-treated by refluxing with 15 mL 85% $HNO_3$ at 80 °C for 1 h, washed until pH 7, dried at 110 °C for 24 h, and finely ground.

### 2.3 Preparation of biochar-incorporated $TiO_2$ (BC-$TiO_2$) composite

BC-$TiO_2$ was synthesized following a wet precipitation method. Acid-treated TSB (0.1 g) was dispersed in isopropanol (3.76 mL), followed by dropwise addition of TTIP (97%, 0.376 mL) under sonication (40 °C water bath, 2 h). The mixture was heated to 80 °C for solvent evaporation, with residual solvent removed by

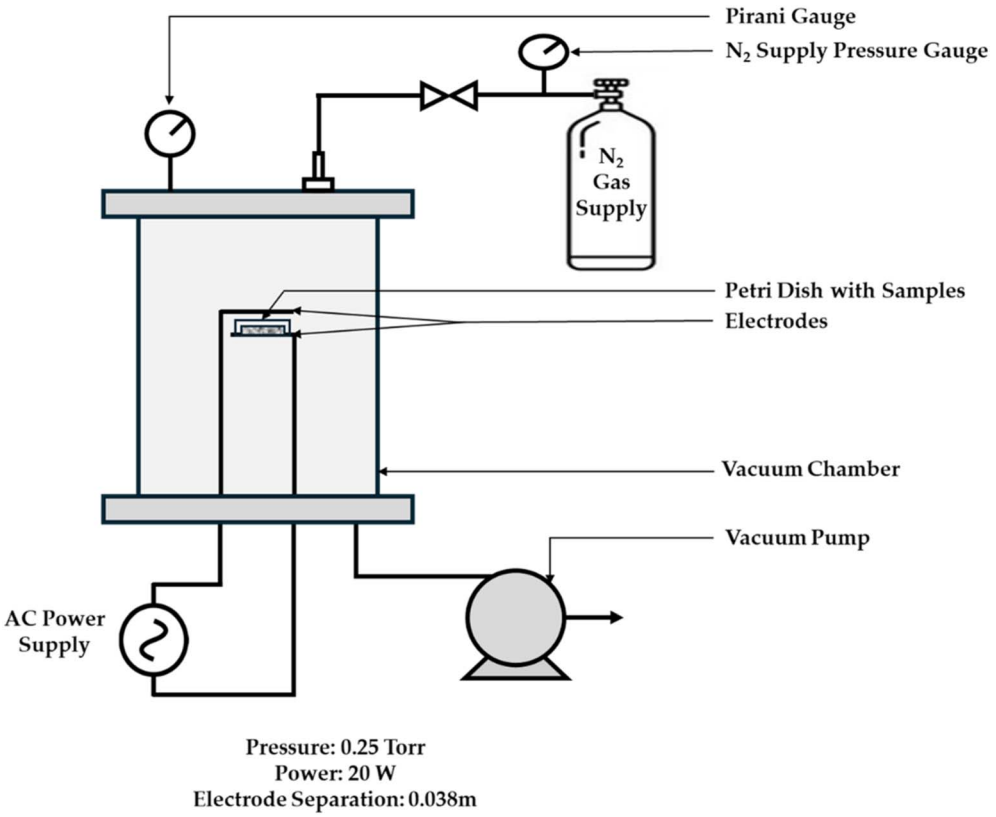


Fig. 1 AC plasma doping system for nitrogen functionalization of biochar-$TiO_2$ composites.

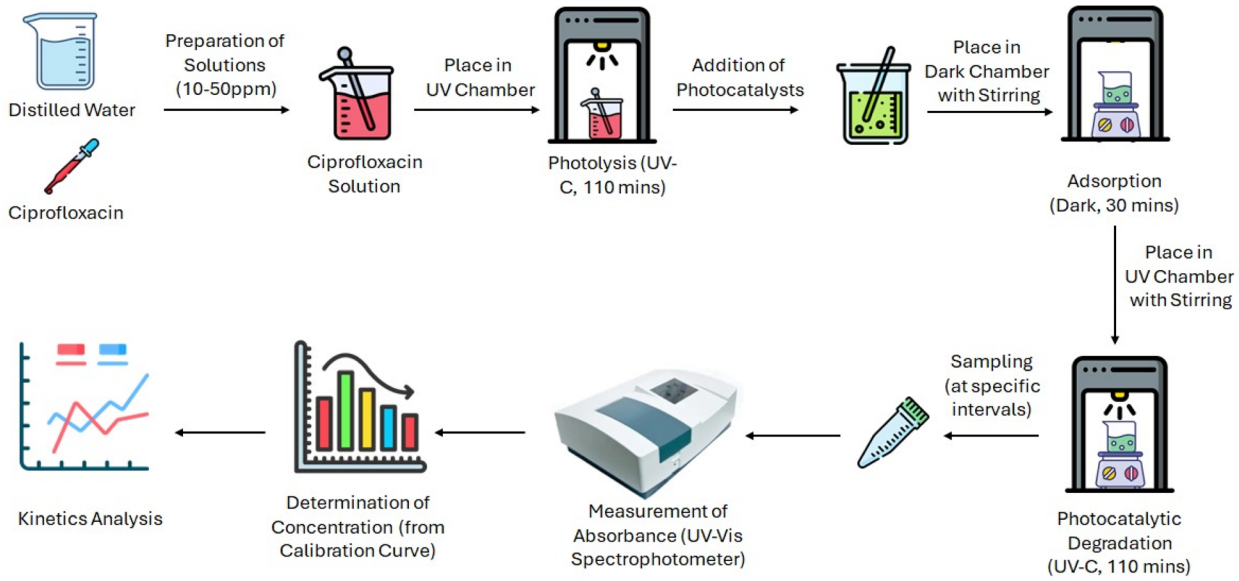


Fig. 2 Experimental protocol for ciprofloxacin photodegradation: CIP solution preparation (10–50 mg $L^{-1}$), photolysis control (UV-C, 254 nm, 110 min), catalyst addition (500 mg $L^{-1}$)/dark adsorption (30 min), photocatalytic degradation with timed sampling, and UV-vis quantification (276 nm).

drying at 85 °C for 4 h. The solid was ground and calcined under $N_2$ flow (10 L $min^{-1}$) at 450 °C for 2 h (5 °C per min ramp).

### 2.4 Nitrogen plasma doping

Nitrogen-doped BC-$TiO_2$ nanocomposites were synthesized *via* AC plasma treatment in a custom vacuum system equipped with parallel copper electrodes (separation: 0.038 m), a quartz chamber, $N_2$ gas supply with pressure regulation, Pirani gauge (operating pressure: 0.25 Torr), rotary vane vacuum pump, and AC power supply (50 Hz, 20 W) as displayed in Fig. 1. Samples were uniformly dispersed in a Petri dish positioned on the grounded electrode. The chamber underwent evacuation (10 min) followed by dynamic $N_2$ purging (99.999% purity, 20 L $min^{-1}$). Plasma was ignited at 20 W for 15 min under continuous $N_2$ flow, after which samples were cooled in an $N_2$ atmosphere and stored in amber vials to prevent photodegradation prior to characterization.

### 2.5 Characterization of materials

Surface morphology and elemental composition were analyzed using Scanning Electron Microscopy (SEM; Zeiss EVO18) coupled with Energy Dispersive X-ray Spectroscopy (EDX). Powder samples mounted on carbon-coated aluminum stubs were imaged at 10 kV acceleration voltage (15 000–70 000× magnification). EDX area scans quantified elemental distributions of Ti, O, C, and N across ≥ 5 regions per sample to assess doping homogeneity. Crystalline phase identification and structural analysis were performed by X-ray Diffraction (XRD; Rigaku SmartLab SE) with Cu Kα radiation ($\lambda = 1.5406$ Å). Scans covered 10–80° ($2\theta$) at 2° $min^{-1}$ (step size 0.02°), enabling crystallite size calculation using Scherrer's equation (eqn (1)), lattice strain calculation using Williamson–Hall approach, and phase determination (anatase *vs.* rutile).

$$D = \frac{k\lambda}{\beta \cos \theta} \quad (1)$$

where $\lambda$ is the X-ray wavelength of the incident beam (0.154 nm), $\theta$ is the Bragg angle, $k$ is the crystallite-shape factor (0.9), and $\beta$ is the full width at half maximum (FWHM) of the diffraction peak in radians.

Particle size distributions in suspension were determined by Dynamic Light Scattering (DLS). Samples (10 mg $L^{-1}$ in DI water) were sonicated for 30 min and measured in triplicate at 25 °C, reporting intensity-weighted hydrodynamic diameters. Optical properties and photocatalytic degradation were monitored *via* UV-vis spectroscopy (Shimadzu UV 2600). Bandgap energies were derived from diffuse reflectance spectra (DRS).

### 2.6 Quantitative kinetics evaluation of ciprofloxacin photodegradation

Ciprofloxacin (CIP) degradation kinetics were systematically evaluated to assess the photocatalytic efficacy of synthesized catalysts. Aqueous CIP solutions were prepared at five discrete initial concentrations (10, 20, 30, 40, and 50 mg $L^{-1}$). Photocatalysis reactions were conducted in a UV irradiation chamber equipped with 10 UV-C emission sources ($\lambda = 254$ nm; irradiance = 15 mW $cm^{-2}$). Prior to catalytic testing, photolysis controls were performed by subjecting catalyst-free CIP solutions to 110 min of continuous UV exposure under magnetic stirring (500 rpm) to quantify inherent photodegradation. For photocatalytic experiments, 500 mg $L^{-1}$ of each material was added to fresh ciprofloxacin (CIP) solutions. The suspensions were exposed to UV light, and samples were collected at specific time intervals for analysis. Samples underwent immediate centrifugation to separate the catalyst, followed by a 10-fold dilution of supernatants. Residual CIP concentrations were determined spectrophotometrically (Shimadzu UV-2600i) at $\lambda_{max} = 276$ nm, referenced against a five-point

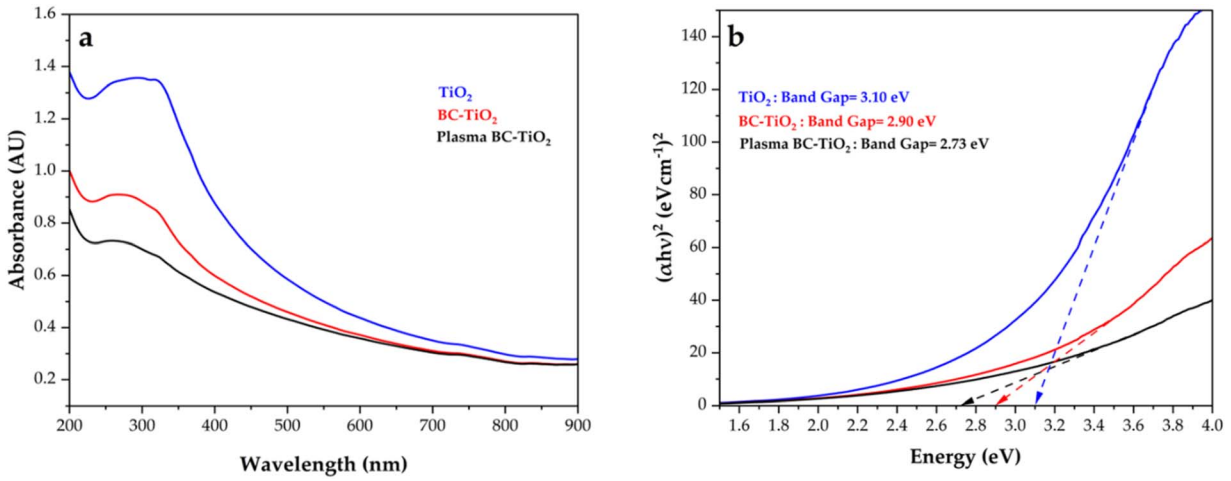


Fig. 3 (a) UV-vis diffuse reflectance spectra (DRS) of synthesized photocatalysts: pristine $TiO_2$, biochar-supported $TiO_2$ (BC-$TiO_2$), and plasma-doped nitrogen-functionalized biochar-$TiO_2$ (plasma BC-$TiO_2$), (b) Tauc plots for bandgap of $TiO_2$ (3.10 eV), BC-$TiO_2$ (2.90 eV), plasma BC-$TiO_2$ (2.73 eV).

calibration curve ($R^2 \geq 0.998$) constructed from standard solutions. A schematic of the experimental protocol is shown in Fig. 2.

Degradation efficiency ($\eta$, %) was calculated using eqn (2) as mentioned below.

$$\eta(\%)\frac{C_o - C}{C_o} \times 100\% \quad (2)$$

where $C_o$ is the initial antibiotic concentration, and $C$ is the concentration at time $t$. Langmuir–Hinshelwood (L–H) kinetics is widely employed to model the photodegradation of organic pollutants using $TiO_2$ and modified $TiO_2$ composites.[35] This model accounts for both adsorption and surface reaction dynamics, where the rate-limiting step is often the generation or attack of hydroxyl radicals ($^{\bullet}OH$),[36] while adsorption significantly influences overall efficiency.[37] The L–H rate equation is expressed by eqn (3) as reported below.

$$-\frac{dC}{dt} = \frac{kKC}{1 + KC} \quad (3)$$

where $C$ is the ciprofloxacin (CIP) concentration at time $t$, $k$ is the reaction rate constant, and $K$ is the adsorption equilibrium coefficient. For dilute solutions ($KC \ll 1$), eqn (3) simplifies to pseudo-first-order kinetics as indicated in eqn (4).[38]

$$\ln\frac{C}{C_0} = kKt = k_{app}t \quad (4)$$

Conversely, at high CIP concentrations ($KC \gg 1$), the reaction will be zero-order kinetics dominate, which can be expressed by eqn (5).[39]

$$C_0 - C = k_{app}t \quad (5)$$

# 3. Results and discussions

## 3.1 Visual appearance of the synthesized photocatalysts

Synthesized materials exhibited distinct macroscopic color variations (Table S1), providing preliminary evidence of structural modifications. Pristine $TiO_2$ appeared as a bright white powder. Characteristic of a high-purity anatase phase with minimal defect states.[15] Biochar incorporation induced a yellowish-brown hue in BC-$TiO_2$, attributed to carbon-mediated charge transfer complexes and partial $Ti^{4+}$ reduction.[18] Plasma-treated BC-$TiO_2$ exhibited pronounced gray coloration, a definitive indicator of successful nitrogen doping *via* creation of $Ti^{3+}$ species and oxygen vacancies.[25]

## 3.2 UV-vis DRS analysis of the photocatalysts

UV-vis diffuse reflectance spectroscopy revealed progressive absorption edge redshifts from $TiO_2$ ($\lambda$_edge $\approx$ 394 nm) to BC-$TiO_2$ ($\lambda$_edge $\approx$ 420 nm) to plasma BC-$TiO_2$ ($\lambda$_edge $\approx$ 450 nm), indicating significant bandgap narrowing from 3.10 eV ($TiO_2$) to 2.90 eV (BC-$TiO_2$) and ultimately 2.73 eV (plasma BC-$TiO_2$) (Fig. 3). The 0.20 eV reduction in BC-$TiO_2$ originates from interfacial interactions between $TiO_2$ and the $\pi$-conjugated system of biochar, which may facilitate electron delocalization and charge transfer across the composite interface.[18] Concurrently, biochar serves as an electron reservoir, suppressing recombination by extending charge carrier lifetimes.[14] The most substantial bandgap reduction (0.37 eV) occurred in plasma BC-$TiO_2$, resulting from synergistic mechanisms as nitrogen doping probably introduced mid-gap states through Ti–O–N bond formation,[25] while plasma-induced oxygen vacancies created localized states below the conduction band.[40] These modifications, combined with defect-mediated light harvesting of biochar,[30] collectively enhance visible light absorption. Although direct photoluminescence or EIS measurements were not performed due to resource constraints, the substantially improved photocatalytic activity of plasma BC-$TiO_2$ and its reduced bandgap strongly suggest diminished electron–hole recombination. This phenomenon is attributed to nitrogen dopants increasing crystallite dimensions (as confirmed by XRD) and creating efficient electron trapping sites,[41] where mid-gap states localize photogenerated electrons to improve charge

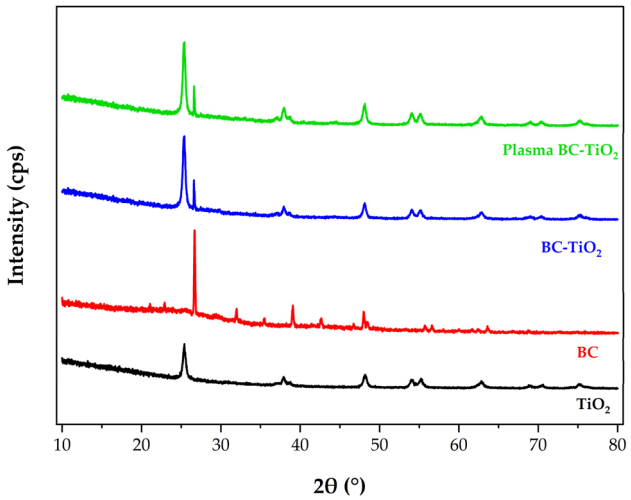


Fig. 4 X-ray diffraction analysis (XRD) pattern of titanium dioxide ($TiO_2$), biochar incorporated titanium dioxide (BC $TiO_2$), and biochar incorporated plasma doped nitrogen titanium dioxide (plasma BC $TiO_2$).

separation.[42] Critically, the modified band structure retains thermodynamically favorable redox potentials: the conduction band shift facilitates efficient electron transfer to $O_2$ for $^{\bullet}O_2^-$ formation, while the valence band remains sufficiently positive to oxidize $H_2O/OH^-$ into $^{\bullet}OH$ radicals.[43] Notably, pure biochar was excluded from DRS analysis due to its inherent optical characteristics, as Urbach tails from structural disorder can distort band edge determination,[44] while dominant absorption from $\pi \rightarrow \pi^*$ transitions and surface defects provides unreliable bandgap data.[45] This progressive bandgap engineering directly correlates with enhanced photocatalytic activity under visible light irradiation.

### 3.3 XRD analysis

X-ray diffraction analysis (Fig. 4) revealed distinct crystallographic features across the synthesized materials. Pristine $TiO_2$ nanoparticles exhibited characteristic anatase phase diffraction patterns, with a dominant peak at 25.3° (101 planes) and secondary peaks at 48.0° (200), 36.9° (103), 37.8° (004), 53.9° (105), 55.1° (211), 62.7° (204), 68.8° (116), 70.3° (220), and 75.0° (215). These peak positions align precisely with standard anatase references (JCPDS # 88-1175 and # 84-1286). The absence of any detectable signal at 27.5°, which is the characteristic rutile (110) reflection, confirms synthesized $TiO_2$ phase purity, consistent with calcination temperatures below the anatase-to-rutile transition threshold.[46] The sharp peak profiles

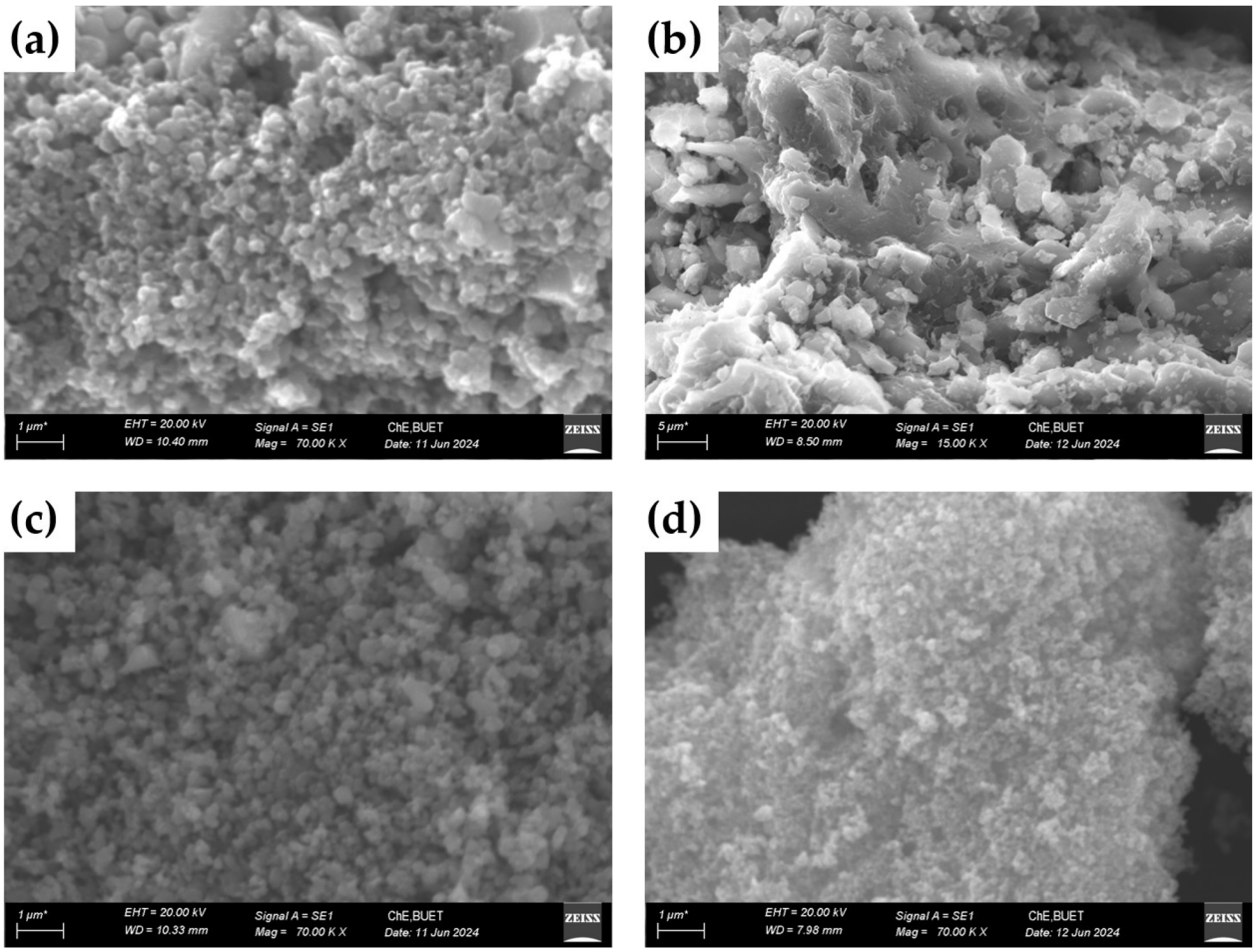


Fig. 5 Scanning electron microscopy analysis of (a) $TiO_2$, (b) biochar, (c) biochar supported $TiO_2$, and (d) plasma doped biochar supported $TiO_2$.

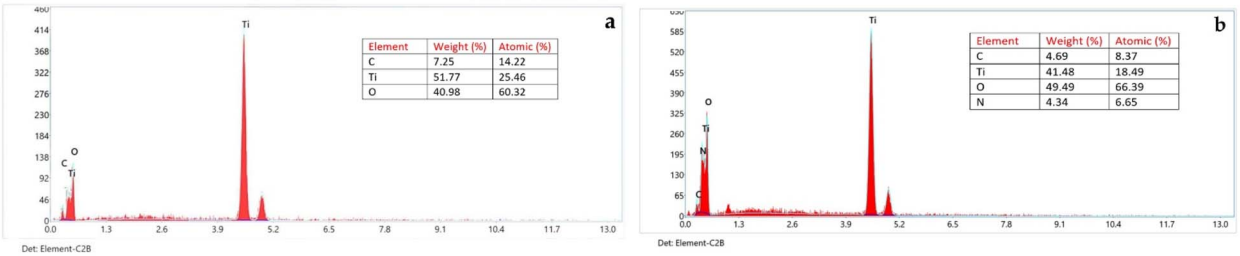


Fig. 6 Elemental composition of C, N, O, and Ti in (a) biochar supported $TiO_2$, and (b) plasma doped biochar supported $TiO_2$.

indicate high crystallinity,[47] a critical attribute for photocatalytic performance.[48]

The anatase structure demonstrated ideal band energetics for photocatalysis: a conduction band edge at −0.5 V *vs.* NHE facilitates efficient $O_2$ reduction to superoxide radicals ($^{\bullet}O_2^-$, $E^\circ$ = −0.33 V), while a valence band at +2.7 V *vs.* NHE enables thermodynamically favorable oxidation of $H_2O$ to hydroxyl radicals ($^{\bullet}OH$, $E^\circ$ = +2.27 V) and $OH^-$ to $^{\bullet}OH$ ($E^\circ$ = +1.99 V).[49] This band alignment promotes effective charge separation, essential for radical-mediated degradation.

Biochar exhibited a broad amorphous hump between 20 and 30°, attributed to disordered carbon structures,[50] additionally, superimposed with discrete crystalline peaks at 22.0°, 26.5°, and 32.0–64.0°. The BC-$TiO_2$ composite retained all anatase peaks while displaying the distinctive biochar reflection at 26.5°,[51] confirming successful hybridization without phase alteration.

Critically, plasma-treated plasma BC-$TiO_2$ maintained identical peak positions and phases despite confirmed nitrogen incorporation (EDX: 6.65 wt%). The absence of peak shifting or new phases indicates nitrogen occupied interstitial sites (Ti–O–N) or substitutional positions without disrupting the $TiO_2$ lattice.[52] This preservation of crystallographic integrity while achieving doping is a key advantage of plasma processing. Scherrer analysis of the XRD peak broadening yielded crystallite sizes of 15.30 nm for $TiO_2$, 46.93 nm for biochar, 16.68 nm for BC-$TiO_2$, and 15.84 nm for plasma BC-$TiO_2$. The nanoscale dimensions (<20 nm) of the $TiO_2$-based samples provide high surface-to-volume ratios that enhance reactive site accessibility.[53] Notably, the plasma treatment induced only a marginal increase in crystallite size (15.30 nm to 15.84 nm), indicating preservation of the $TiO_2$ morphological framework while achieving electronic modification through nitrogen incorporation. In contrast, a monotonic increase in lattice strain ($\varepsilon$) values (biochar, $1.38 \times 10^{-4}$ < $TiO_2$, $3.52 \times 10^{-4}$ < BC-$TiO_2$, $7.87 \times 10^{-4}$ < plasma BC-$TiO_2$, $11.14 \times 10^{-4}$), suggests the lattice distortion was affected by defect generation and interfacial stress.[54] Plasma treatment introduced the highest micro strain despite preserving the crystallographic integrity of BC-$TiO_2$, attributed to the synergistic effects of plasma induced oxygen vacancies, $Ti^{3+}$ defect formation in the $TiO_2$ lattice, mismatched lattice distortions at $TiO_2$-biochar interface, and enhanced surface functionalization by plasma treatment.[55,56] The superlative lattice strain in plasma BC-$TiO_2$ provides effective charge trapping sites, subsequently enhancing the charge separation and photocatalytic activity[54]

### 3.4 Morphological and elemental characterization *via* SEM-EDX

Scanning electron microscopy revealed distinct morphological features across synthesized materials (Fig. 5). Pristine $TiO_2$ nanoparticles formed clustered aggregates of irregular-to-spherical particles (Fig. 5a), exhibiting characteristic cauliflower-like surface textures consistent with sol–gel synthesis.[57] This morphology indicates high surface energy, conducive to enhanced reactivity and efficient charge carrier transfer.[58]

Biochar displayed a highly porous network with rough, layered surfaces (Fig. 5b), suggesting a high surface area beneficial for the adsorption of antibiotics and catalyst support.[59] The BC-$TiO_2$ composite showed well-dispersed $TiO_2$ nanoparticles anchored within this porous biochar matrix (Fig. 5c), creating packed interfacial contacts that facilitate electron transfer and reactant accessibility. Plasma BC-$TiO_2$ exhibited denser $TiO_2$ distributions with reduced particle sizes (~100 nm *via* DLS correlation), suggesting nitrogen functionalization enhanced interfacial interactions and nucleation stability (Fig. 5d). This morphological refinement aligns with plasma-

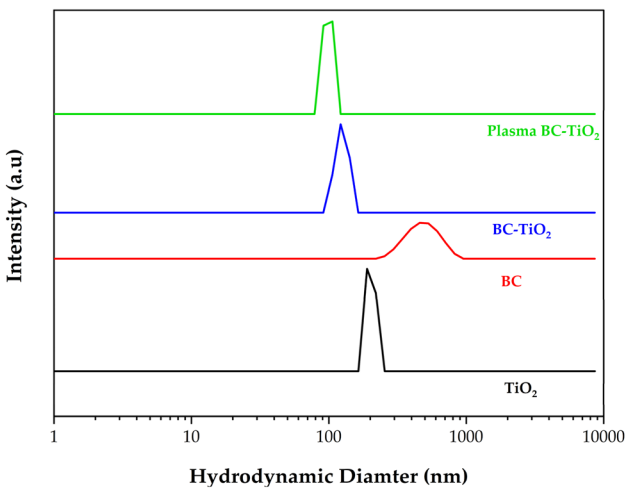


Fig. 7 Dynamic light scattering analysis of $TiO_2$, biochar (BC), biochar supported $TiO_2$ (BC-$TiO_2$), and plasma doped biochar supported $TiO_2$ (plasma BC-$TiO_2$) particles.

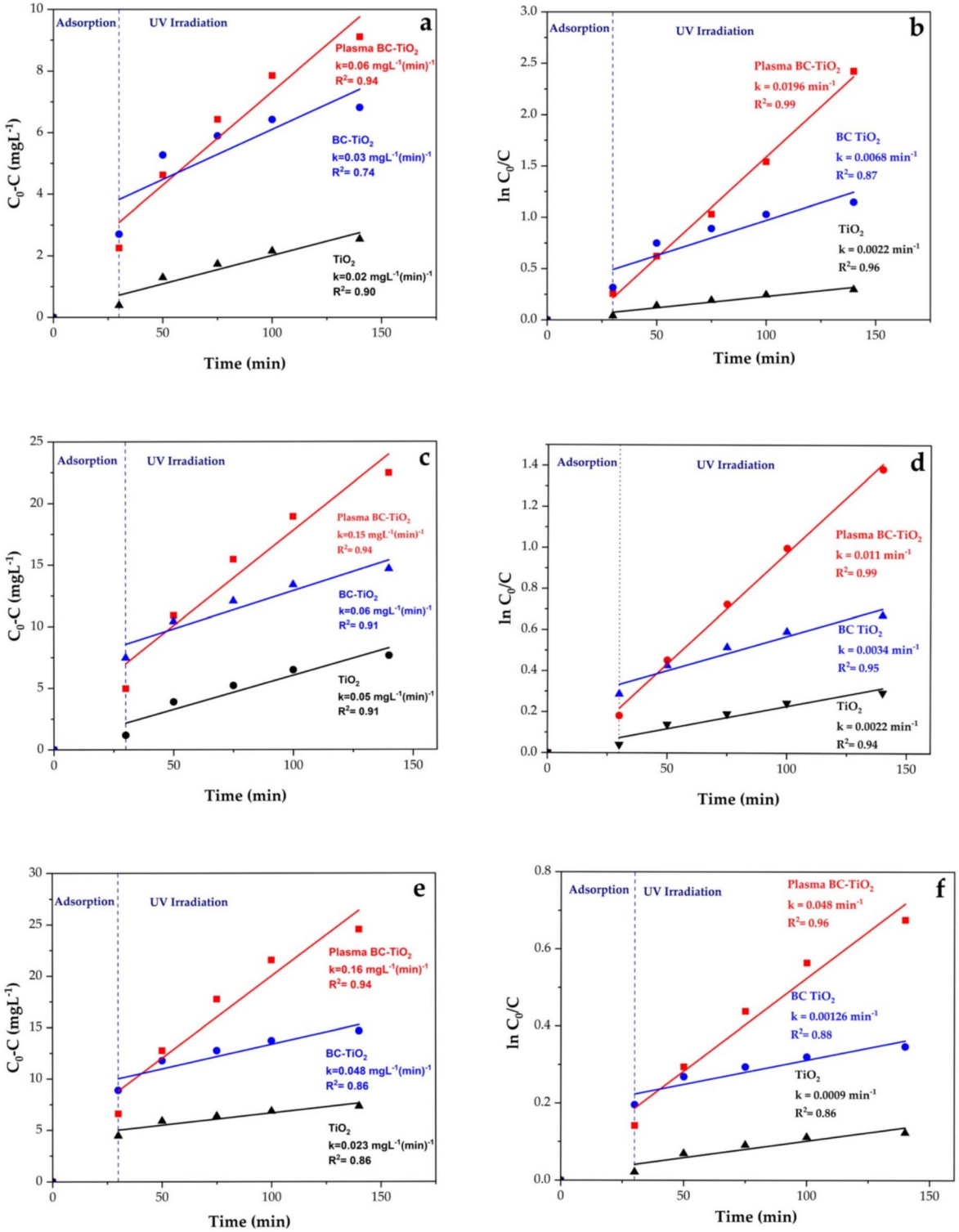


Fig. 8 Kinetic analysis of CIP degradation: (a, c, and e) zero-order and (b, d, and f) pseudo-first-order models for $TiO_2$, BC-$TiO_2$, and plasma BC-$TiO_2$ at 10, 30, and 50 ppm CIP.

induced surface modification, promoting stronger $TiO_2$-biochar integration.

Complementary EDX analysis quantified elemental distributions (Fig. 6). BC-$TiO_2$ showed moderate carbon content (14.22 wt%, Fig. 6), confirming partial $TiO_2$ coverage of the biochar substrate while maintaining an accessible carbon matrix. Even though XPS analysis could not be performed due to resource limitations, plasma BC-$TiO_2$ demonstrated successful nitrogen incorporation (6.65 wt%, Fig. 6) in EDX analysis, with N/Ti/O atomic ratios supporting interstitial doping configurations (Ti–O–N) through oxygen site substitution. This nitrogen integration facilitates visible-light activation through N-$TiO_2$

formation, as confirmed by a reduced bandgap of 2.73 eV (UV-vis DRS).

### 3.5 Hydrodynamic size distribution analysis *via* DLS

DLS measurements revealed distinct particle dynamics across the synthesized photocatalysts (Fig. 7). For pristine $TiO_2$, bimodal size distributions (190–220 nm) confirmed moderate aggregation, consistent with the clustered morphologies observed *via* SEM. This residual agglomeration likely stems from the high surface energy of sol–gel synthesized $TiO_2$ nanoparticles. Biochar exhibited broad polydispersity (255–825 nm), with dominant populations at 400–600 nm reflecting incomplete size fractionation during post-pyrolysis processing. Crucially, sieving and grinding enabled BC-$TiO_2$ composites to achieve remarkably uniform dispersions (106–142 nm). This size refinement indicates successful fragmentation of biochar supports and homogeneous $TiO_2$ anchoring, key factors in minimizing charge migration distances and suppressing recombination. Plasma BC-$TiO_2$ maintained bimodality but within an exceptionally narrow distribution (90–106 nm). This represents a clear improvement over BC-$TiO_2$ and suggests nitrogen functionalization actively stabilizes dispersions. This can be attributed to plasma-generated surface sites that enhance $TiO_2$ anchoring on biochar, a phenomenon supported by a recent study of doped semiconductor interfaces.[60]

### 3.6 Kinetics of ciprofloxacin degradation

In dark conditions, pristine $TiO_2$ exhibited minimal adsorption due to its inherent low porosity and lack of functional groups (Fig. 8). By contrast, biochar-supported composites (BC-$TiO_2$ and plasma BC-$TiO_2$) demonstrated enhanced adsorption, with BC-$TiO_2$ ($K$ = 0.001–0.0015 $min^{-1}$ from L–H model, Table S2) outperforming plasma BC-$TiO_2$ ($K$ = 0.00098–0.001 $min^{-1}$ from L–H model, Table S2) across all CIP concentrations. This reduction in adsorption for plasma-treated samples is attributed to plasma-induced alterations in surface chemistry, including pore etching, modified surface charge, and degradation of functional groups.[61] Under UV irradiation, kinetic analysis revealed high linearity ($R^2 \geq$ 0.93–0.99) and close agreement between L–H and pseudo-first-order (PFO) $k_{app}$ values (Table S2), indicating adsorption-controlled pseudo-first-order degradation behavior at low CIP concentrations (10 mg $L^{-1}$) for all catalysts (Fig. 8b). Plasma BC-$TiO_2$ achieved the highest apparent rate constant ($k_{app}$ = 0.0196 $min^{-1}$), exceeding BC-$TiO_2$ by ~three times and pristine $TiO_2$ by ~nine times. At intermediate concentrations (30 mg $L^{-1}$), all catalysts maintained good fit with pseudo-first order kinetics as evidenced by comparable L-H and PFO parameters in Table S2. Plasma BC-$TiO_2$ maintained superior kinetics ($k_{app}$ = 0.011 $min^{-1}$), tripling the efficiency of BC-$TiO_2$ ($k_{app}$ = 0.0034 $min^{-1}$) and quintupling that of $TiO_2$ ($k_{app}$ = 0.0022 $min^{-1}$). At 50 mg $L^{-1}$, the declining $R^2$ values for L–H model ($TiO_2$: 0.566, BC-$TiO_2$: 0.64, plasma-BC-$TiO_2$: 0.89) and comparable $R^2$ values for pseudo-first and zero-order models (Fig. 8(e and f)) indicated a transition between kinetic regimes, driven by limited $^{\bullet}OH/^{\bullet}O_2^-$ generation. Despite this shift, plasma BC-$TiO_2$ consistently demonstrated the highest degradation efficiency under each model, followed by BC-$TiO_2$. The exceptional performance of plasma BC-$TiO_2$ arises from synergistic effects, *e.g.*, biochar-enhanced adsorption facilitates CIP proximity to active sites; nitrogen doping narrows the bandgap from 2.90 eV (BC-$TiO_2$) to 2.73 eV, enhancing UV-light absorption; and probable dopant-induced electron-trapping sites suppress charge recombination.[42] Despite its lower carbon content, plasma BC-$TiO_2$ outperformed BC-$TiO_2$ due to Ti–O–N/Ti–N–O configurations that optimize reactive oxygen species (ROS) generation. The narrowed bandgap likely shifts the conduction band edge negatively, favoring $^{\bullet}O_2^-$ production *via* $O_2$ reduction, while valence band holes oxidize $H_2O/OH^-$ to $^{\bullet}OH$.[43] Although scavenging experiments were not conducted, established literature confirms that $TiO_2$-based catalysts generate $^{\bullet}OH$ and $^{\bullet}O_2^-$ under UV,[39] and their synergistic action drives the observed enhancement.

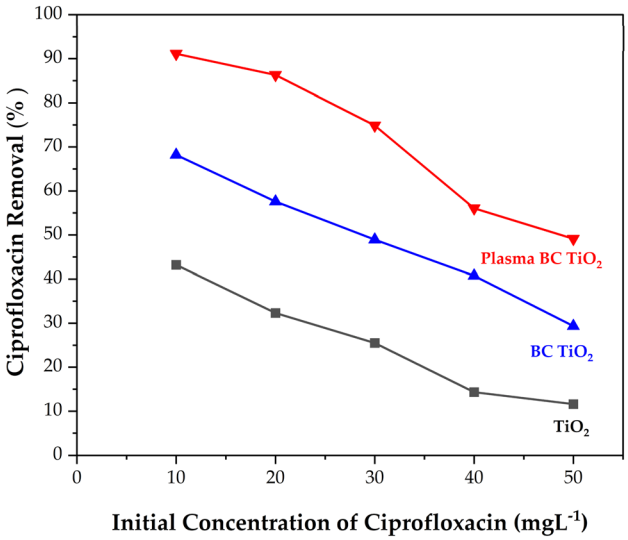


Fig. 9 Degradation efficiency of catalysts *vs.* initial CIP concentration.

### 3.7 Influence of ciprofloxacin concentration on photocatalytic efficiency

The initial concentration of ciprofloxacin (CIP) critically influences photocatalytic degradation efficiency, as evidenced by systematic evaluation across five concentrations (10–50 mg $L^{-1}$), revealing an inverse relationship where efficiency declines with increasing CIP concentration due to photon path reduction from heightened molecular density, limiting UV penetration,[62] saturation of finite catalyst active sites, leaving undegraded CIP molecules,[62] UV attenuation and scattering by CIP ($\lambda_{max}$ = 276 nm) suppressing $^{\bullet}OH/^{\bullet}O_2^-$ generation,[63] and diffusion-limited mass transfer diminishing the concentration gradient at the catalyst–solution interface.[64] Nevertheless, plasma BC-$TiO_2$ consistently outperformed BC-$TiO_2$ and pristine $TiO_2$ across all concentrations (Fig. 9), achieving >40% and >70% higher degradation than BC-$TiO_2$ and $TiO_2$, respectively, at 50 mg $L^{-1}$ after 140 min, attributable to synergistic bandgap narrowing (2.73 eV), enhanced charge separation, and

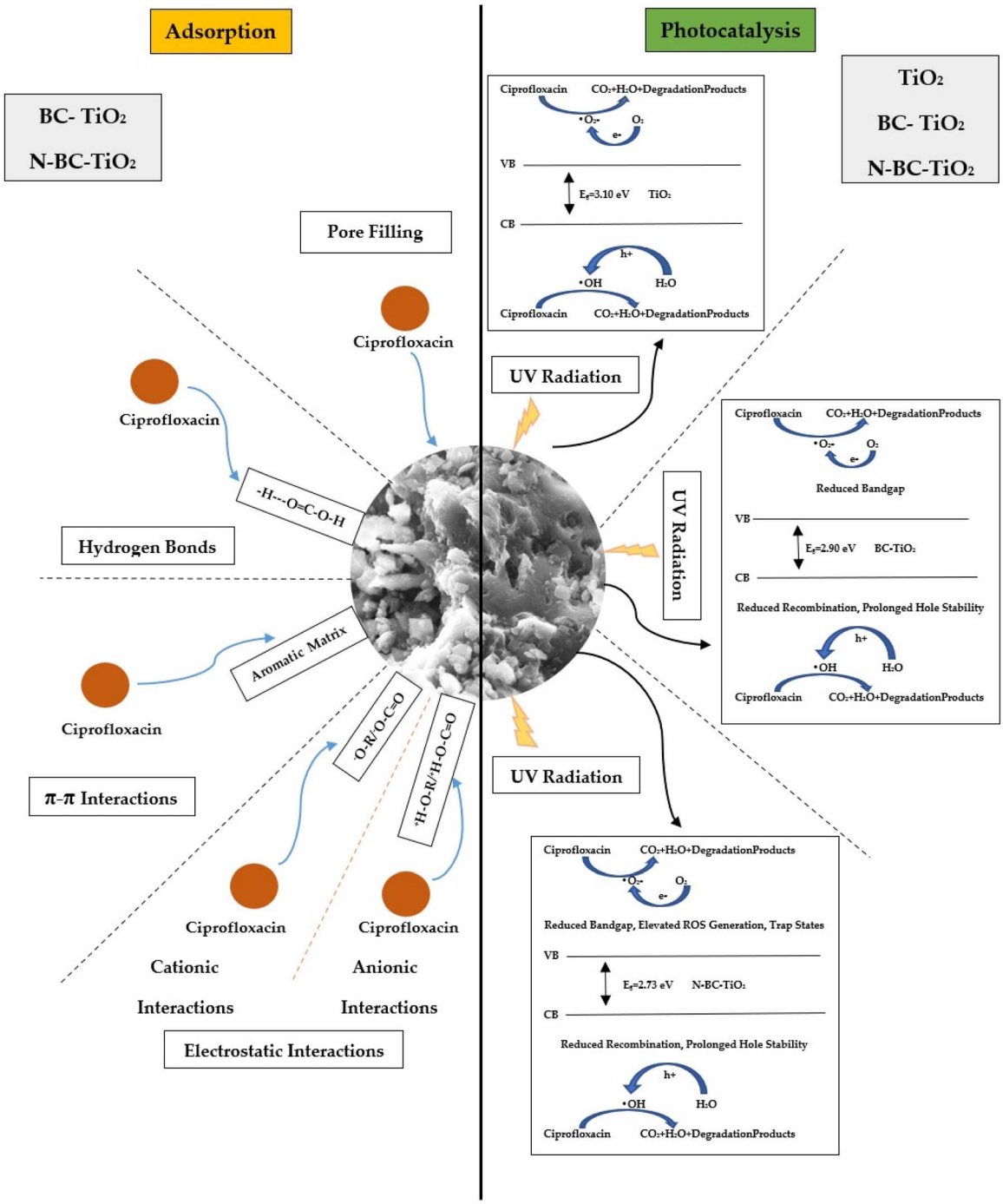


Fig. 10 Schematic representation of adsorption, charge transfer dynamics, and radical-mediated degradation pathways for ciprofloxacin over plasma-functionalized biochar-$TiO_2$ nanocomposites.

sustained ROS generation *via* nitrogen doping (6.65 wt%) and biochar-mediated adsorption, validating its hierarchical superiority for CIP remediation under diffusion-limited conditions.[42]

### 3.8 Proposed mechanistic pathways for ciprofloxacin mineralization

The photocatalytic degradation pathway of ciprofloxacin (CIP) initiates with adsorption phenomena, where pristine $TiO_2$ exhibits inherently limited capacity for hydrophobic CIP molecules due to insufficient porosity and surface functional groups.[65] Incorporation of textile sludge-derived biochar significantly enhances adsorption through four concurrent mechanisms: (i) physical entrapment within micropores and mesopores of the biochar matrix, (ii) hydrogen bonding between oxygenated moieties (–OH, C=O) on biochar and amine/carbonyl groups of CIP, (iii) π–π stacking interactions between graphitic domains of biochar and aromatic rings in

Table 1 Comparison with recent studies on N-doped $TiO_2$ and biochar-based photocatalysts

| Study (author, year) | Catalyst design strategy | Material origin/ support | Modification approach | Light source | Pollutant | Catalyst loading (mg $L^{-1}$) | Irradiation time (min) | Performance of catalysts | Kinetic matrices | Novelty (this study)/ comparison with this work |
|---|---|---|---|---|---|---|---|---|---|---|
| $N_2$ plasma doped biochar supported $TiO_2$ (this study) | Plasma N-doped BC-$TiO_2$ | Textile-sludge biochar | AC plasma N-doping on biochar-supported $TiO_2$ | UV-C (254 nm) | Ciprofloxacin | 500 | 140 (30 min dark + 110 min UV) | 91.1% for 10 mg $L^{-1}$ CIP | L–H model, PFO, zero-order comparison | Unique plasma-biochar synergy with comprehensive kinetic analysis |
| Ashebir *et al.* (2025)[74] | N-doped $TiO_2$/ biochar | Urea ($CH_4N_2O$) and prosopis juliflora biochar | Sol–gel technique | UV and sunlight | Ciprofloxacin | 2000 | 30 min dark + 120 min UV | 98% for 50 mg $L^{-1}$ | PFO $k_{app}$ = 0.023 $min^{-1}$ | Low surface control, a long period of deposition |
| Ashebir *et al.* (2025)[75] | N-doped $TiO_2$/ biochar | Urea ($CH_4N_2O$) and prosopis juliflora biochar | Sol–gel technique | UV and sunlight | Ciprofloxacin, sulfamethoxazole | 1500 | 30 min dark + 120 min UV | ~95% for 50 mg $L^{-1}$ CIP ~97% for 50 mg $L^{-1}$ SFX | N/A | Low surface control, a long period of deposition |
| Alharbi *et al.* (2025)[76] | $TiO_2$/biochar composite | Red sea algae biochar | Spin-coating process | Visible light | Methylene blue | 500 | 30 min dark + 150 min UV | 84% for 10 mg $L^{-1}$ CIP | PFO $k_{app}$ = 0.0127–0.0214 $min^{-1}$ | No $N_2$ doping No plasma synthesis, lower degradation efficiency |
| Xiong *et al.* (2023)[60] | N-doped $TiO_2$/N-biochar | Walnut shell biochar | Direct hydrolysis | UV (360 nm) | Methyl orange | 250 | 60 min dark + 90 min UV | 97.6% for 20 mg $L^{-1}$ | PFO $k_{app}$ = 0.042 $min^{-1}$ | High heat treatment and high-temperature calcination required |
| Onwubiko *et al.* (2024)[77] | $TiO_2$–C–N composite | Pluronic F108 | Sol-hydrothermal synthesis | UV light (365 nm) | Methylene blue | 100 | 1 hour dark + 1 hour UV | 99.8% for 50 mg $L^{-1}$ | PFO $k_{app}$ = 0.02 $min^{-1}$ | High energy input required, long reaction time (for dark) required |
| Beaudette *et al.* (2022)[78] | N-doped $TiO_2$ | Tetrakis (dimethylamido) titanium (TDMAT) | Nonthermal plasma process | Natural light clear sky irradiation | Methyl orange (MO) Methylene blue (MB) | 100 | 120 in dark + 120 min sunlight | ~70% for 2 × $10^{-4}$ M MB ~75% for 1 × $10^{-4}$ M MO | N/A | Disordered band structure and low adsorption capacity with biochar integration. Lower degradation efficiency |

quinolone core of CIP, and (iv) pH-dependent electrostatic attraction/repulsion at the catalyst–solution interface.[66,67] This multilayer adsorption concentrates CIP proximate to photocatalytic active sites, as visualized in the proposed mechanism in Fig. 10.

Upon UV irradiation ($\lambda$ = 254 nm, irradiance = 15 mW $cm^{-2}$), photoexcitation occurs across the catalyst bandgap, generating holes ($h^+$) in the valence band (VB) and electrons ($e^-$) in the conduction band (CB) by the following (R1), as evidenced by established studies.[68]

$$TiO_2/BC\text{-}TiO_2/plasma\ BC\text{-}TiO_2 + h\nu \rightarrow h^+(VB) + e^-(CB) \quad (R1)$$

The photogenerated holes oxidize adsorbed water molecules or hydroxyl ions to produce hydroxyl radicals following (R2) and (R3).[69]

$$h^+ + H_2O_{ads} \rightarrow {}^{\bullet}OH + H^+ \quad (R2)$$

$$h^+ + OH_{ads}{}^- \rightarrow {}^{\bullet}OH \quad (R3)$$

Concurrently, electrons reduce dissolved molecular oxygen to superoxide radicals following (R4) as substantiated by electron paramagnetic resonance studies in analogous systems.[43]

$$e^- + O_2(aq) \rightarrow {}^{\bullet}O_2 \quad (R4)$$

Conjugated $sp^2$-carbon network of biochar functions as an electron shuttle, accepting and delocalizing $e^-$ from $TiO_2$ to suppress recombination, thereby extending hole lifetimes for sustained $^{\bullet}OH$ generation.[70,71]

Additionally, plasma nitrogen doping introduces atomic nitrogen (6.65 wt% confirmed by EDX) into the $TiO_2$ lattice, forming Ti–O–N configurations that narrow the bandgap from 2.90 eV (BC-$TiO_2$) to 2.73 eV (plasma BC-$TiO_2$) by mid-gap states below the conduction band (Fig. 3).[72] This modification enhances visible-light absorption and creates electron traps that further inhibit $e^-/h^+$ recombination.[70] The modified band structure retains thermodynamically favorable redox potentials: the CB edge (−0.45 V *vs.* NHE) facilitates $O_2$ reduction to $^{\bullet}O_2{}^-$ ($E^\circ$ = −0.33 V), while the VB (+2.75 V *vs.* NHE) enables water oxidation to $^{\bullet}OH$ ($E^\circ$ = +2.27 V).[60]

Scholarly evidence confirmed that the reactive oxygen species ($^{\bullet}OH$, $^{\bullet}O_2{}^-$, $H_2O_2$) mineralize adsorbed ciprofloxacin through three competitive degradation pathways, as substantiated by prior mechanistic studies.[73] Defluorination initiates *via* nucleophilic $^{\bullet}OH$ attack at the C8–F bond of the quinolone ring, substituting fluorine to yield 8-hydroxyciprofloxacin. Concurrently, decarboxylation proceeds through radical-mediated cleavage of the C3-carboxylic group (–COOH), releasing $CO_2$ and generating desethylene-ciprofloxacin. The piperazine ring cleavage pathway involves $^{\bullet}O_2{}^-$-driven oxidation of the C7–N bond, fragmenting the piperazine moiety into *N*-ethylenediamine and ketone intermediates. These primary degradation products undergo sequential oxidation, forming formaldehyde and formic acid as transient species, before ultimate mineralization to $CO_2$ and $H_2O$.[73] Although LC-MS/MS analysis was not executed in this study to identify transient intermediates due to instrumental limitations, established literature confirms that decarboxylation and piperazine cleavage dominate over defluorination due to their lower activation barriers, reflecting thermodynamic favorability.[73] The hierarchical degradation efficiency (plasma BC-$TiO_2$ > BC-$TiO_2$ > $TiO_2$) emerges from synergistic interactions: biochar's porous structure enhances CIP adsorption proximity, its conductive π-network prolongs charge carrier lifetimes by suppressing $e^-/h^+$ recombination, and plasma-induced nitrogen doping optimizes band energetics for maximal ROS flux at the catalyst–pollutant interface.

## 4. Comparative analysis

The current study exhibits several clear strengths while also having identifiable limitations that warrant transparent discussion. The primary strength of this study lies in its catalyst design strategy, which integrates AC plasma assisted nitrogen doping with textile sludge biochar-supported $TiO_2$. This approach enables controlled surface and electronic modification without prolonged high temperature calcination or extended precursor deposition, distinguishing it from conventional sol–gel or hydrothermal routes reported in comparable studies. In addition, the use of waste derived biochar enhances the sustainability profile of the catalyst and introduces adsorption functionality that synergistically complements photocatalytic degradation. Moreover, the work is strengthened by the application of a comprehensive kinetic framework, including Langmuir–Hinshelwood, pseudo-first-order, and zero-order models, allowing explicit consideration of adsorption–reaction that is largely absent in prior reports, which typically rely on pseudo-first-order kinetics alone (Table 1). From a performance perspective, the plasma-BC-$TiO_2$ catalyst demonstrates high degradation efficiency (91.1%) for ciprofloxacin at 10 mg $L^{-1}$ using a moderate catalyst loading (500 mg $L^{-1}$), which is lower than the loadings required in several sol–gel-based biochar $TiO_2$ systems to achieve comparable efficiencies. However, the study also has its limitations. The photocatalytic evaluation was conducted exclusively under UV-C irradiation (254 nm), which constrains direct comparison with studies reporting visible light or solar driven activity and limits conclusions regarding solar applicability. Moreover, while the degradation efficiency is competitive, it is achieved at a lower pollutant concentration than some literature reports, and mineralization metrics (*e.g.*, TOC removal), and catalyst reusability measurements were not assessed. Although plasma modification offers advantages in surface control, the scalability and energy cost of plasma processing relative to conventional thermal methods require proper evaluation. Even though the limitations primarily relate to irradiation conditions and the scope of performance validation, this approach provides integrated design, sustainability, and kinetic depth.

## 5. Conclusion

This work establishes nitrogen plasma-functionalized biochar-$TiO_2$ composite as a high-performance photocatalyst, where the strategic integration of textile sludge-derived biochar with AC

plasma doping unlocks synergistic enhancement in antibiotic degradation. Systematic characterization confirms that plasma-induced nitrogen incorporation reduces the bandgap from 3.10 eV to 2.73 eV while preserving anatase crystallinity, enabling extended visible-light absorption and suppressing charge recombination through tailored mid-gap states. Critically, hierarchical porosity and reduced hydrodynamic diameters facilitate superior reactant diffusion to active sites, while the biochar matrix serves as both an electron reservoir and an adsorption scaffold. The ambient-temperature plasma treatment demonstrates exceptional energy efficiency, maintaining >40% degradation efficiency at diffusion-limited ciprofloxacin concentrations (50 mg $L^{-1}$) and achieving 9-fold kinetics enhancement over pristine $TiO_2$. Beyond immediate performance metrics, this approach redefines sustainable materials design paradigms: it transforms textile waste into functional defect-engineered composites through a scalable, low-carbon manufacturing route. The methodology establishes a blueprint for next-generation photocatalytic systems targeting refractory aquatic contaminants, simultaneously addressing industrial waste valorization and water remediation challenges within circular economy frameworks.

## Author contributions

Conceptualization: H. R., and M. S. I.; data curation: R. B. M., S. R. A., H. R., M. J. R., and M. S. I.; formal analysis: R. B. M., S. R. A., and H. R; funding acquisition: M. J. R., and M. S. I.; investigation: R. B. M., S. R. A., and H. R.; methodology: R. B. M., S. R. A., and H. R; project administration: H. R., and M. S. I.; supervision: H. R., and M. S. I.; validation: M. J. R., and M. S. I.; writing – original draft: R. B. M., S. R. A., and H. R., writing – review & editing: R. B. M., S. R. A., H. R., and S. I.

## Conflicts of interest

There are no conflicts to declare.

## Data availability

Supplementary information (SI) is available. See DOI: https://doi.org/10.1039/d5ra09288d.

## Acknowledgements

The authors would like to thank the technical support received from the Bangladesh University of Engineering and Technology (BUET) and the financial support received from the Bangladesh Bureau of Educational Information and Statistics (BANBEIS) under the project ID: ET20232849.

## References

1 A. Nikolaou, S. Meric and D. Fatta, Occurrence patterns of pharmaceuticals in water and wastewater environments, *Anal. Bioanal. Chem.*, 2007, **387**(4), 1225–1234, DOI: 10.1007/s00216-006-1035-8.

2 P. E. Stackelberg, E. T. Furlong, M. T. Meyer, S. D. Zaugg, A. K. Henderson and D. B. Reissman, Persistence of pharmaceutical compounds and other organic wastewater contaminants in a conventional drinking-water-treatment plant, *Sci. Total Environ.*, 2004, **329**(1–3), 99–113, DOI: 10.1016/j.scitotenv.2004.03.015.

3 E. S. Elmolla and M. Chaudhuri, The feasibility of using combined TiO2 photocatalysis-SBR process for antibiotic wastewater treatment, *Desalination*, 2011, **272**(1–3), 218–224, DOI: 10.1016/j.desal.2011.01.020.

4 M. V. Walter and J. W. Vennes, Occurrence of multiple-antibiotic-resistant enteric bacteria in domestic sewage and oxidation lagoons, *Appl. Environ. Microbiol.*, 1985, **50**(4), 930–933, DOI: 10.1128/aem.50.4.930-933.1985.

5 S. R. Andersen, Effects of waste water treatment on the species composition and Antibiotic resistance of coliform bacteria, *Curr. Microbiol.*, 1993, **26**(2), 97–103, DOI: 10.1007/BF01577343.

6 A. Kumar and D. Pal, Antibiotic resistance and wastewater: Correlation, impact and critical human health challenges, *J. Environ. Chem. Eng.*, 2018, **6**(1), 52–58, DOI: 10.1016/j.jece.2017.11.059.

7 A. Novo and C. M. Manaia, Factors influencing antibiotic resistance burden in municipal wastewater treatment plants, *Appl. Microbiol. Biotechnol.*, 2010, **87**(3), 1157–1166, DOI: 10.1007/s00253-010-2583-6.

8 A. Safarzadeh-Amiri, J. R. Bolton and S. R. Cater, The Use of Iron in Advanced Oxidation Processes, *J. Adv. Oxid. Technol.*, 1996, **1**(1), DOI: 10.1515/jaots-1996-0105.

9 Y. Deng and R. Zhao, Advanced Oxidation Processes (AOPs) in Wastewater Treatment, *Curr. Pollut. Rep.*, 2015, **1**(3), 167–176, DOI: 10.1007/s40726-015-0015-z.

10 R. Dewil, D. Mantzavinos, I. Poulios and M. A. Rodrigo, New perspectives for Advanced Oxidation Processes, *J. Environ. Manage.*, 2017, **195**, 93–99, DOI: 10.1016/j.jenvman.2017.04.010.

11 L. Zhu, X. Tian, G. Shi, *et al.*, Assembling 3D cross-linked network by carbon nitride nanowires for visible-light photocatalytic H2 evolution from dyestuffs wastewater, *Chin. Chem. Lett.*, 2025, **36**(12), 111088, DOI: 10.1016/j.cclet.2025.111088.

12 T. U. Rahman, H. Roy, A. Fariha, *et al.*, Progress in plasma doping semiconductor photocatalysts for efficient pollutant remediation and hydrogen generation, *Sep. Purif. Technol.*, 2023, **320**, 124141, DOI: 10.1016/j.seppur.2023.124141.

13 Z. N. Kayani, R. S. Maria and S. Naseem, Magnetic and antibacterial studies of sol-gel dip coated Ce doped TiO2 thin films: Influence of Ce contents, *Ceram. Int.*, 2020, **46**(1), 381–390, DOI: 10.1016/j.ceramint.2019.08.272.

14 S. Na Phattalung, S. Limpijumnong and J. Yu, Passivated co-doping approach to bandgap narrowing of titanium dioxide with enhanced photocatalytic activity, *Appl. Catal. B Environ.*, 2017, **200**, 1–9, DOI: 10.1016/j.apcatb.2016.06.054.

15 F. Ling, W. Li and L. Ye, The synergistic effect of non-metal doping or defect engineering and interface coupling on the photocatalytic property of g-C3N4: First-principle

investigations, *Appl. Surf. Sci.*, 2019, **473**, 386–392, DOI: 10.1016/j.apsusc.2018.12.085.

16 S. Islam, S. Nagpure, D. Kim and S. Rankin, Synthesis and Catalytic Applications of Non-Metal Doped Mesoporous Titania, *Inorganics*, 2017, **5**(1), 15, DOI: 10.3390/inorganics5010015.

17 R. Marschall and L. Wang, Non-metal doping of transition metal oxides for visible-light photocatalysis, *Catal. Today*, 2014, **225**, 111–135, DOI: 10.1016/j.cattod.2013.10.088.

18 S. Banerjee, S. C. Pillai, P. Falaras, K. E. O'Shea, J. A. Byrne and D. D. Dionysiou, New Insights into the Mechanism of Visible Light Photocatalysis, *J. Phys. Chem. Lett.*, 2014, **5**(15), 2543–2554, DOI: 10.1021/jz501030x.

19 M. R. Al-Mamun, S. Kader, M. S. Islam and M. Z. H. Khan, Photocatalytic activity improvement and application of UV-TiO2 photocatalysis in textile wastewater treatment: A review, *J. Environ. Chem. Eng.*, 2019, **7**(5), 103248, DOI: 10.1016/j.jece.2019.103248.

20 A. Islam, Y. H. Taufiq-Yap, C. M. Chu, E. S. Chan and P. Ravindra, Synthesis and characterization of millimetric gamma alumina spherical particles by oil drop granulation method, *J. Porous Mater.*, 2012, **19**(5), 807–817, DOI: 10.1007/s10934-011-9535-0.

21 B. Pant, M. Park and S. J. Park, Recent Advances in TiO2 Films Prepared by Sol-Gel Methods for Photocatalytic Degradation of Organic Pollutants and Antibacterial Activities, *Coatings*, 2019, **9**(10), 613, DOI: 10.3390/coatings9100613.

22 W. Zhang, X. Chen, X. Zhao, M. Yin, L. Feng and H. Wang, Simultaneous nitrogen doping and Cu2O oxidization by one-step plasma treatment toward nitrogen-doped Cu2O@CuO heterostructure: An efficient photocatalyst for H2O2 evolution under visible light, *Appl. Surf. Sci.*, 2020, **527**, 146908, DOI: 10.1016/j.apsusc.2020.146908.

23 A. Ramos-Corona, R. Rangel, J. Lara-Romero and A. Ramos-Carrazco, Nitrogen-plasma doped ZnO-graphene oxide compounds production and their photocatalytic performance, *Adv. Powder Technol.*, 2022, **33**(11), 103829, DOI: 10.1016/j.apt.2022.103829.

24 S. Hosseini and A. Amoozadeh, Plasma Treatment as a Promising Environmentally Benign Approach for Synthesis of Valuable Multi-gas Doped Nano-TiO2-P25: An Efficient Way to Boost the Photocatalytic Performance under Visible Light Illumination, *Photochem. Photobiol.*, 2021, **97**(4), 672–687, DOI: 10.1111/php.13374.

25 H. U. Lee, Y. C. Lee, S. C. Lee, *et al.*, Visible-light-responsive bicrystalline (anatase/brookite) nanoporous nitrogen-doped TiO2 photocatalysts by plasma treatment, *Chem. Eng. J.*, 2014, **254**, 268–275, DOI: 10.1016/j.cej.2014.06.011.

26 R. Trejo-Tzab, J. J. Alvarado-Gil, P. Quintana and P. Bartolo-Pérez, N-doped TiO2 P25/Cu powder obtained using nitrogen (N2) gas plasma, *Catal. Today*, 2012, **193**(1), 179–185, DOI: 10.1016/j.cattod.2012.01.003.

27 R. Trejo-Tzab, J. J. Alvarado-Gil and P. Quintana, Photocatalytic Activity of Degussa P25 TiO2/Au Obtained Using Argon (Ar) and Nitrogen (N2) Plasma, *Top. Catal.*, 2011, **54**(1–4), 250–256, DOI: 10.1007/s11244-011-9643-8.

28 C. Chen, H. Bai and C. Chang, Effect of Plasma Processing Gas Composition on the Nitrogen-Doping Status and Visible Light Photocatalysis of TiO $_2$, *J. Phys. Chem. C*, 2007, **111**(42), 15228–15235, DOI: 10.1021/jp0716233.

29 S. F. Jiang, L. L. Ling, Z. Xu, W. J. Liu and H. Jiang, Enhancing the Catalytic Activity and Stability of Noble Metal Nanoparticles by the Strong Interaction of Magnetic Biochar Support, *Ind. Eng. Chem. Res.*, 2018, **57**(39), 13055–13064, DOI: 10.1021/acs.iecr.8b02777.

30 M. Pinna, G. Binda, M. Altomare, *et al.*, Biochar Nanoparticles over TiO2 Nanotube Arrays: A Green Co-Catalyst to Boost the Photocatalytic Degradation of Organic Pollutants, *Catalysts*, 2021, **11**(9), 1048, DOI: 10.3390/catal11091048.

31 J. Liu, J. Jiang, Y. Meng, *et al.*, Preparation, environmental application and prospect of biochar-supported metal nanoparticles: A review, *J. Hazard. Mater.*, 2020, **388**, 122026, DOI: 10.1016/j.jhazmat.2020.122026.

32 S. A. Iqbal, I. Mahmud and A. K. M. A. Quader, Textile Sludge Management by Incineration Technique, *Procedia Eng.*, 2014, **90**, 686–691, DOI: 10.1016/j.proeng.2014.11.795.

33 D. Guo, Y. Li, B. Cui, *et al.*, Natural adsorption of methylene blue by waste fallen leaves of Magnoliaceae and its repeated thermal regeneration for reuse, *J. Cleaner Prod.*, 2020, **267**, 121903, DOI: 10.1016/j.jclepro.2020.121903.

34 T. B. Anwar, B. Behrose and S. Ahmed, Utilization of textile sludge and public health risk assessment in Bangladesh, *Sustainable Environ. Res.*, 2018, **28**(5), 228–233, DOI: 10.1016/j.serj.2018.04.003.

35 C. Mounir, H. Ahlafi, M. Aazza, H. Moussout and S. Mounir, Kinetics and Langmuir–Hinshelwood mechanism for the catalytic reduction of para-nitrophenol over Cu catalysts supported on chitin and chitosan biopolymers, *React. Kinet., Mech. Catal.*, 2021, **134**(1), 285–302, DOI: 10.1007/s11144-021-02066-w.

36 C. Mounir, H. Ahlafi, M. Aazza, H. Moussout and S. Mounir, Kinetics and Langmuir–Hinshelwood mechanism for the catalytic reduction of para-nitrophenol over Cu catalysts supported on chitin and chitosan biopolymers, *React. Kinet., Mech. Catal.*, 2021, **134**(1), 285–302, DOI: 10.1007/s11144-021-02066-w.

37 O. Benhabiles, H. Mahmoudi, H. Lounici and M. F. A. Goosen, Effectiveness of a photocatalytic organic membrane for solar degradation of methylene blue pollutant, *Desalin. Water Treat.*, 2016, **57**(30), 14067–14076, DOI: 10.1080/19443994.2015.1061954.

38 M. El-Kemary, H. El-Shamy and I. El-Mehasseb, Photocatalytic degradation of ciprofloxacin drug in water using ZnO nanoparticles, *J. Lumin.*, 2010, **130**(12), 2327–2331, DOI: 10.1016/j.jlumin.2010.07.013.

39 T. Hayri-Senel, E. Kahraman, S. Sezer, N. Erdol-Aydin and G. Nasun-Saygili, Photocatalytic degradation of ciprofloxacin from water with waste polystyrene and TiO2 composites, *Heliyon*, 2024, **10**(3), e25433, DOI: 10.1016/j.heliyon.2024.e25433.

40 K. Takeuchi, I. Nakamura, O. Matsumoto, S. Sugihara, M. Ando and T. Ihara, Preparation of Visible-Light-

Responsive Titanium Oxide Photocatalysts by Plasma Treatment, *Chem. Lett.*, 2000, **29**(12), 1354–1355, DOI: 10.1246/cl.2000.1354.

41 R. Asahi, T. Morikawa, T. Ohwaki, K. Aoki and Y. Taga, Visible-Light Photocatalysis in Nitrogen-Doped Titanium Oxides, *Science*, 2001, **293**(5528), 269–271, DOI: 10.1126/science.1061051.

42 Y. Ye, Y. Feng, H. Bruning, D. Yntema and H. H. M. Rijnaarts, Photocatalytic degradation of metoprolol by TiO2 nanotube arrays and UV-LED: Effects of catalyst properties, operational parameters, commonly present water constituents, and photo-induced reactive species, *Appl. Catal. B Environ.*, 2018, **220**, 171–181, DOI: 10.1016/j.apcatb.2017.08.040.

43 Q. Zhang, G. Rao, J. Rogers, C. Zhao, L. Liu and Y. Li, Novel anti-fouling Fe2O3/TiO2 nanowire membranes for humic acid removal from water, *Chem. Eng. J.*, 2015, **271**, 180–187, DOI: 10.1016/j.cej.2015.02.085.

44 P. M. Chamberlin and K. W. Adu, Determining bandgap from simulated absorbance: The Tauc approach, *MRS Adv.*, 2024, **9**(12), 1031–1036, DOI: 10.1557/s43580-024-00889-y.

45 P. R. Jubu, O. S. Obaseki, D. I. Ajayi, *et al.*, Considerations about the determination of optical bandgap from diffuse reflectance spectroscopy using the tauc plot, *J. Opt.*, 2024, **53**(5), 5054–5064, DOI: 10.1007/s12596-024-01741-0.

46 S. J. Armaković, M. M. Savanović and S. Armaković, Titanium Dioxide as the Most Used Photocatalyst for Water Purification: An Overview, *Catalysts*, 2022, **13**(1), 26, DOI: 10.3390/catal13010026.

47 B. S. Shirke, P. V. Korake, P. P. Hankare, S. R. Bamane and K. M. Garadkar, Synthesis and characterization of pure anatase TiO2 nanoparticles, *J. Mater. Sci.: Mater. Electron.*, 2011, **22**(7), 821–824, DOI: 10.1007/s10854-010-0218-4.

48 L. Zhu, W. Zhang, G. Shi, X. Tian, P. Tang and P. Xia, Synthesizing crystalline g-C3N4 for enhanced photocatalytic hydrogen evolution under visible light, *CrystEngComm*, 2024, **26**(5), 599–603, DOI: 10.1039/D3CE01039B.

49 W. T. Chen, A. Chan, Z. H. N. Al-Azri, *et al.*, Effect of TiO2 polymorph and alcohol sacrificial agent on the activity of Au/TiO2 photocatalysts for H2 production in alcohol–water mixtures, *J. Catal.*, 2015, **329**, 499–513, DOI: 10.1016/j.jcat.2015.06.014.

50 K. Świechowski, W. A. Rasaq, S. Stegenta-Dąbrowska, and A. Białowiec, Characterization of Engineered Biochar: Proximate Analyses, Ultimate Analyses, Physicochemical Analyses, Surface Analyses, and Molecular Analyses, in *Engineered Biochar*, ed. S. Ramola, D. Mohan, O. Masek, A. Méndez, and T. Tsubota, Springer Nature Singapore, 2022, pp. 127–148, DOI: 10.1007/978-981-19-2488-0_8.

51 W. Wang, J. Zhang, T. Chen, *et al.*, Preparation of TiO2-modified Biochar and its Characteristics of Photo-catalysis Degradation for Enrofloxacin, *Sci. Rep.*, 2020, **10**(1), 6588, DOI: 10.1038/s41598-020-62791-5.

52 Q. Chen, A. Ozkan, B. Chattopadhyay, *et al.*, N-Doped TiO $_2$ Photocatalyst Coatings Synthesized by a Cold Atmospheric Plasma, *Langmuir*, 2019, **35**(22), 7161–7168, DOI: 10.1021/acs.langmuir.9b00784.

53 X. Chen and S. S. Mao, Titanium Dioxide Nanomaterials: Synthesis, Properties, Modifications, and Applications, *Chem. Rev.*, 2007, **107**(7), 2891–2959, DOI: 10.1021/cr0500535.

54 W. Qin, T. Nagase, Y. Umakoshi and J. A. Szpunar, Relationship between microstrain and lattice parameter change in nanocrystalline materials, *Philos. Mag. Lett.*, 2008, **88**(3), 169–179, DOI: 10.1080/09500830701840155.

55 U. Chinonso, O. Ibukun and H. Kyung Jeong, Air plasma treated TiO2/MWCNT composite for enhanced photocatalytic activity, *Chem. Phys. Lett.*, 2020, **757**, 137850, DOI: 10.1016/j.cplett.2020.137850.

56 D. Li, K. Xu, Z. Niu, *et al.*, Annealing and Plasma Effects on the Structural and Photocatalytic Properties of TiO2 Fibers Produced by Electrospinning, *Catalysts*, 2022, **12**(11), 1441, DOI: 10.3390/catal12111441.

57 S. Obregón and V. Rodríguez-González, Photocatalytic TiO2 thin films and coatings prepared by sol–gel processing: a brief review, *J. Sol-Gel Sci. Technol.*, 2022, **102**(1), 125–141, DOI: 10.1007/s10971-021-05628-5.

58 S. M. Gupta and M. Tripathi, A review of TiO2 nanoparticles, *Chin. Sci. Bull.*, 2011, **56**(16), 1639–1657, DOI: 10.1007/s11434-011-4476-1.

59 L. Leng, Q. Xiong, L. Yang, *et al.*, An overview on engineering the surface area and porosity of biochar, *Sci. Total Environ.*, 2021, **763**, 144204, DOI: 10.1016/j.scitotenv.2020.144204.

60 Z. Xiong, H. Chen, L. Lu, *et al.*, Nitrogen-Doped $TiO_2$/Nitrogen-Containing Biochar Composite Catalyst as a Photocatalytic Material for the Decontamination of Aqueous Organic Pollutants, *ACS Omega*, 2023, **8**(1), 791–803, DOI: 10.1021/acsomega.2c06127.

61 M. A. Lieberman, and A. J. Lichtenberg, *Principles of Plasma Discharges and Materials Processing*, Wiley, 1st edn, 2005, DOI: 10.1002/0471724254.

62 A. Alam, W. U. Rahman, Z. U. Rahman, *et al.*, Photocatalytic degradation of the antibiotic ciprofloxacin in the aqueous solution using Mn/Co oxide photocatalyst, *J. Mater. Sci.: Mater. Electron.*, 2022, **33**(7), 4255–4267, DOI: 10.1007/s10854-021-07619-2.

63 C. Zong, J. Cui, J. Qu, F. Cheng and Y. nan Zhang, Insights into photodegradation of antibiotics in aquatic environment considering effects of dissolved organic matter and halide ions, *Environ. Earth Sci.*, 2025, **84**(10), 254, DOI: 10.1007/s12665-025-12283-4.

64 T. J. Al-Musawi, N. Mengelizadeh, A. I. Alwared, D. Balarak and R. Sabaghi, Photocatalytic degradation of ciprofloxacin by MMT/CuFe2O4 nanocomposite: characteristics, response surface methodology, and toxicity analyses, *Environ. Sci. Pollut. Res.*, 2023, **30**(27), 70076–70093, DOI: 10.1007/s11356-023-27277-7.

65 M. R. Mulay, and N. Martsinovich, TiO2 Photocatalysts for Degradation of Micropollutants in Water, in *Clean Water and Sanitation. Encyclopedia of the UN Sustainable Development Goals*, ed. W. Leal Filho, A. M. Azul, L. Brandli, A. Lange Salvia, and T. Wall, Springer

International Publishing, 2021, pp. 1–19, DOI: 10.1007/978-3-319-70061-8_194-1.

66 H. Roy, T. R. Prantika, M. H. Riyad, S. Paul and MdS. Islam, Synthesis, characterizations, and RSM analysis of Citrus macroptera peel derived biochar for textile dye treatment, *S. Afr. J. Chem. Eng.*, 2022, **41**, 129–139, DOI: 10.1016/j.sajce.2022.05.008.

67 B. Bems, F. C. Jentoft and R. Schlögl, Photoinduced decomposition of nitrate in drinking water in the presence of titania and humic acids, *Appl. Catal. B Environ.*, 1999, **20**(2), 155–163, DOI: 10.1016/S0926-3373(98)00105-2.

68 A. Hassani, A. Khataee, S. Karaca, C. Karaca and P. Gholami, Sonocatalytic degradation of ciprofloxacin using synthesized TiO2 nanoparticles on montmorillonite, *Ultrason. Sonochem.*, 2017, **35**, 251–262, DOI: 10.1016/j.ultsonch.2016.09.027.

69 H. Zhao, H. Wu, B. Shi, *et al.*, Fast and controllable anatase-to-rutile phase transition irradiated by NIR light, *Chin. Chem. Lett.*, 2025, **36**(11), 110815, DOI: 10.1016/j.cclet.2025.110815.

70 Y. Nosaka and A. Y. Nosaka, Generation and Detection of Reactive Oxygen Species in Photocatalysis, *Chem. Rev.*, 2017, **117**(17), 11302–11336, DOI: 10.1021/acs.chemrev.7b00161.

71 S. Sutar, S. Otari and J. Jadhav, Biochar based photocatalyst for degradation of organic aqueous waste: A review, *Chemosphere*, 2022, **287**, 132200, DOI: 10.1016/j.chemosphere.2021.132200.

72 C. Di Valentin, E. Finazzi, G. Pacchioni, *et al.*, N-doped TiO2: Theory and experiment, *Chem. Phys.*, 2007, **339**(1–3), 44–56, DOI: 10.1016/j.chemphys.2007.07.020.

73 Y. Zhou, C. Huang, L. Yang, *et al.*, Enhanced photodegradation of ciprofloxacin with organic photocatalyst through a ternary strategy, *Energy Mater.*, 2025, **5**, 500010, DOI: 10.20517/energymater.2024.64.

74 H. Ashebir, S. Babaee, A. Worku, P. Diale, T. Msagati and J. F. Nure, N-doped TiO2/prosopis juliflora biochar nanocomposites for removal of ciprofloxacin from pharmaceutical industrial wastewater, *Sci. Rep.*, 2025, **15**(1), 31795, DOI: 10.1038/s41598-025-03330-y.

75 H. Ashebir, S. Babaee, P. Diale, A. Worku, T. Msagati and J. F. Nure, The application of N-doped TiO2-biochar nanocomposite for photocatalytic degradation of ciprofloxacin and Sulfamethoxazole in real wastewater, *Mater. Sci. Eng., B*, 2026, **323**, 118735, DOI: 10.1016/j.mseb.2025.118735.

76 F. F. Alharbi, T. A. Hamdalla, H. Al-Ghamdi, *et al.*, Biochar-Modified TiO2 Composites: Enhanced Optical and Photocatalytic Properties for Sustainable Energy and Environmental Applications, *Catalysts*, 2025, **15**(11), 1065, DOI: 10.3390/catal15111065.

77 V. Onwubiko, Y. Matsushita, E. A. Elshehy and M. E. El-Khouly, Facile synthesis of TiO2–carbon composite doped nitrogen for efficient photodegradation of noxious methylene blue dye, *RSC Adv.*, 2024, **14**(46), 34298–34310, DOI: 10.1039/D4RA05444J.

78 C. A. Beaudette, Q. Tu, M. Ali Eslamisaray and U. R. Kortshagen, Plasma-Synthesized Nitrogen-Doped Titanium Dioxide Nanoparticles With Tunable Visible Light Absorption and Photocatalytic Activity, *ASME Open J. Eng.*, 2022, **1**, 011010, DOI: 10.1115/1.4053338.